



**SETCOR**  
Conferences & Exhibitions

**The SMS/NanoMed/Sensors/EGF 2022  
International Joint Conference**

**Oct 26 to 28, 2022, Athens, Greece  
Conference Proceedings**

**DOI:**

**<https://doi.org/10.26799/cp-sms-egf-nanomed-sensors-2022>**

# Computational Assessment of Three-Dimensional Scaffolds for Bone Regeneration

Ourania Ntousi<sup>1</sup>, Maria Roumpi<sup>1</sup>, Panagiotis Siogkas<sup>1</sup>, Dimitrios I. Fotiadis<sup>1,2</sup>

<sup>1</sup>Unit of Medical Technology and Intelligent Information Systems, University of Ioannina, Ioannina, Greece

<sup>2</sup>Biomedical Research Institute-FORTH, Ioannina, Greece

## Abstract

During the past years, tissue engineering has been qualified as a solid surrogate of autografts in the stimulation of bone tissue regeneration, through the development of three dimensional (3D) porous matrices, commonly known as scaffolds. Polycaprolactone-based scaffolds have attracted worldwide attention as promising biodegradable implants in bone tissue engineering. Finite Element Analysis is used in tissue engineering to evaluate the mechanical behaviour and to simulate the processes inside the scaffold. In this work, we analysed two regular polycaprolactone scaffold structures (with sharp edges and with rounded edges) by performing computational fluid dynamics simulations, to compare velocity and pressure distributions for the two scaffolds. A sensitivity analysis was performed for the two different scaffold geometries and the element size that was used was 0.07mm. A laminar flow 1 mm/s was used as an inlet boundary condition at the top of the scaffolds and the fluid was treated as Newtonian [1, 2]. Our results indicate that the scaffold with sharp edges depicted a better flow velocity distribution within the pores of the scaffold for all layers and a lower speed, compared to the scaffold with rounded edges. The pressure gradually decreases from the inlet to the outlet, with no substantial differences between the two geometries, with a uniform pressure distribution along the height of the scaffolds. Based on the Computational Fluid Dynamics derived results, the rounded edges geometry produced more appealing velocity distribution results which makes it superior compared to the sharp edges scaffold.

**Keywords:** Bone regeneration, Scaffold, finite element analysis, fluid flow.

## 1. Introduction

In recent years, the incorporation of porous polycaprolactone-based scaffolds in regeneration and healing of damaged organs attracted the attention of researchers in the tissue engineering. Tissue engineering scaffolds are key components because they provide the appropriate environment and three-dimensional structure for cells to attach, proliferate, differentiate, and secrete its own extracellular matrix. [3]

The scaffold properties are mainly determined by the following three factors: material, structure, and fabrication technique. The three-dimensional (3D) scaffold pore architecture is an important design parameter, as it affects not only the mechanical properties, but also the capability for cells to penetrate the scaffold and for nutrients, oxygen and waste products to diffuse through the scaffold. Scaffold structure significantly determines its porosity and stiffness. However, changing the scaffold structure could lead to a conflict between its porosity and stiffness. More specifically, the higher porosity a scaffold has, the lower stiffness it usually possesses [3].

Finite element analysis (FEA) has been evaluated as a powerful tool for computational fluid dynamics (CFD) as an effective alternative to complex and expensive experimental tests in fluid behavior investigations. In numerical analysis techniques, such as FEA and CFD, computer-aided design (CAD) models are commonly used, but the manufacturing-induced differences between these models and actual scaffolds are often ignored. In general, computational methods for scaffold design not only improve the traditional process of fabricating scaffolds, more importantly, it opens a new way in tissue engineering, which provides researchers with a wide and flexible range of choices to design and optimize scaffolds [4, 5].

Existing research has mainly focused on the scaffolds design of which are used to simulate the process by which a fluid flows through the cross-sections of the scaffold and how it diffuses. The pore shape of the scaffold plays a decisive role in cell growth. Abraham et. al. [1] performed a fluid flow analysis to determine the fluid behavior of the implant scaffolds in the environment of synovial fluid with different materials and pore shape. From the results of the analysis of static loading condition and material comparison, the equivalent stress produced in the pores of scaffold model plays an important role in selection of the material. The research of Deng et. al [2] based

on computational fluid dynamics (CFD) analysis, the permeability, velocity, and flow trajectory inside the scaffold structure were calculated. The internal fluid velocity difference of the DIA structure is the smallest, and the trajectory of fluid flow inside the scaffold is the longest, which is beneficial for blood vessel growth, nutrient transport and bone formation. Jusoh et. al. [6] indicate that the variations in pore sizes affected significantly the scaffold permeability.

In this study, we analyzed two regular polycaprolactone scaffold structures employ the computational fluid dynamics simulation, to compare velocity and pressure distributions for the proposed scaffold geometries.

## 2. Materials and Methods

### 2.1 Scaffold Models

Two groups of polycaprolactone scaffolds cubes with a size of 12x12x12mm were designed using Solidworks™ with sharp edges and with rounded edges, and with a 60% porosity, pores dimensions 1.029x0.8mm and strut dimensions of 0.6x0.8mm (Fig.1). The porosity of the scaffold is the percentage of the structure in a complete solid:

$$(1) \quad (1 - V_p)/V_s$$

where  $V_p$  is the volume of the structural unit and  $V_s$  is the volume of the complete solid.

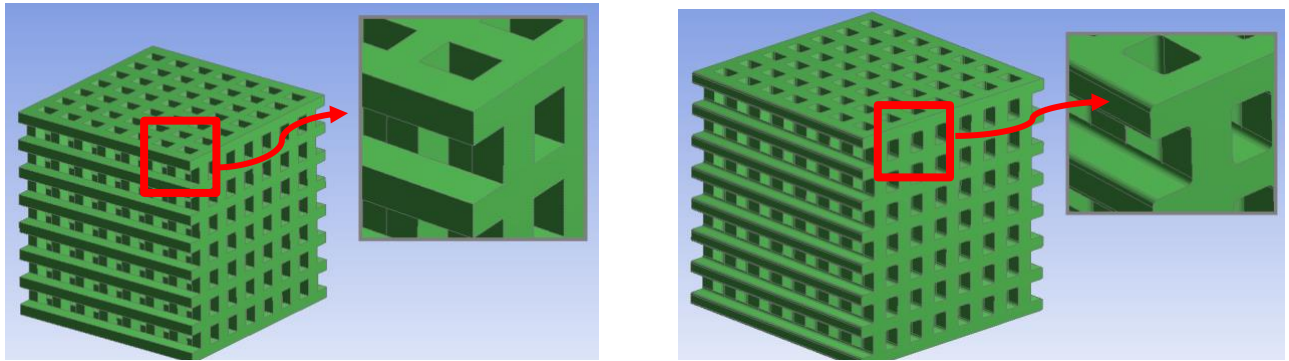


**Fig. 1:** (a) Geometry with sharp edges and (b) geometry with rounded edges. The scaffold is a cube with dimensions 12x12x12mm. The pores have dimensions 1.029x0.8mm and the strut 0.6x0.8mm.

### 2.2 CFD Analysis

The two scaffold geometries were imported to ANSYS CFX and were analyzed to calculate the pressure and velocity streamline distribution in the structure of the polycaprolactone scaffolds using Computational Fluid Dynamics (CFD), considering the Navier Stokes equation and the continuity equation:

$$\rho \frac{\partial \mathbf{v}}{\partial t} + \rho(\mathbf{v} \cdot \nabla) \mathbf{v} - \nabla \cdot (-p\delta_{ij} + 2\mu\varepsilon_{ij}) = 0, \quad (2)$$

$$\nabla \cdot (\rho \mathbf{v}) = 0,$$

(3)

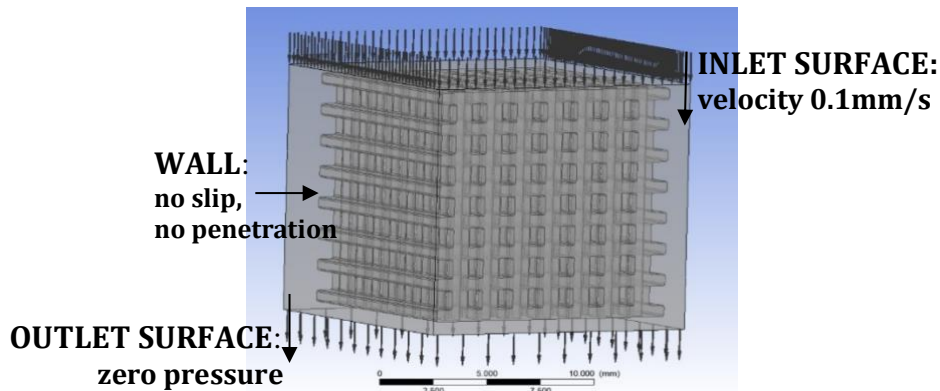
$$\varepsilon_{ij} = \frac{1}{2}(\nabla \mathbf{v} + \nabla \mathbf{v}^T).$$

(4)

where  $\rho$ ,  $v$ , and  $\mu$  represent the fluid density ( $\text{kg/m}^3$ ), velocity of fluid flow (m/s) and dynamic fluid viscosity ( $\text{kg/m/s}$ ), respectively.  $p$  represents the pressure (MPa),  $\delta_{ij}$  is the Kronecker delta and  $\varepsilon_{ij}$  is the strain tensor [7].

Liquid parameters of cell culture medium were used with a density  $1008 \text{ kg/m}^3$ , and viscosity  $0.0078 \text{ kg/m/s}$ . No-penetration wall boundary condition is applied on the surface of the scaffold and on the outside domain. The fluid

inlet velocity is set to 0.1 mm/s, and the outlet pressure is set to 0 Pa. The boundary conditions are shown in Fig. 2. The fluid domain outside of the scaffold is used to avoid boundary effects [6].



### 2.3 Sensitivity Analysis

To obtain accurate results, a mesh sensitivity analysis was performed in a representative case for the rigid wall assumption using steady-state flow. The mesh sensitivity analysis for no slip wall simulation was performed using a face size 0.046–0.2 mm. The analysis was based on the correlation between the mesh size and the produced results regarding the average results of the pressure and the velocity. The mesh size with <5% difference in the parameters values was used in the final simulations. The size of the mesh outside the scaffold region was increased gradually from 0.2 mm to 0.046 mm. Once the mesh was created, the three-dimensional meshing process was common for all cases. We started the discretization using an element face size of 0.2 mm with 381223 elements at the geometry with sharp edges and reached a mesh size of 36.32 million elements with a face element size 0.049 mm with 36.32 million elements. Regarding the rounded edges geometry, the discretization ranged from an element size 0.2 mm which corresponds to 39.77 million elements and an element size 0.046 mm which corresponds to 57.53 million elements [8].

### 3. Results

The flow rate of the fluid in the internal structure of the scaffold has a significant effect on the growth of bone tissue in the scaffold. The pressure distribution and velocity distribution (Fig. 3) for each scaffold at a speed of 0.01 mm/s were calculated. Both scaffolds geometries present a similar static pressure distribution. Each model exhibits a higher static pressure at the inlet surface and gradually decreases towards the outlet surface.

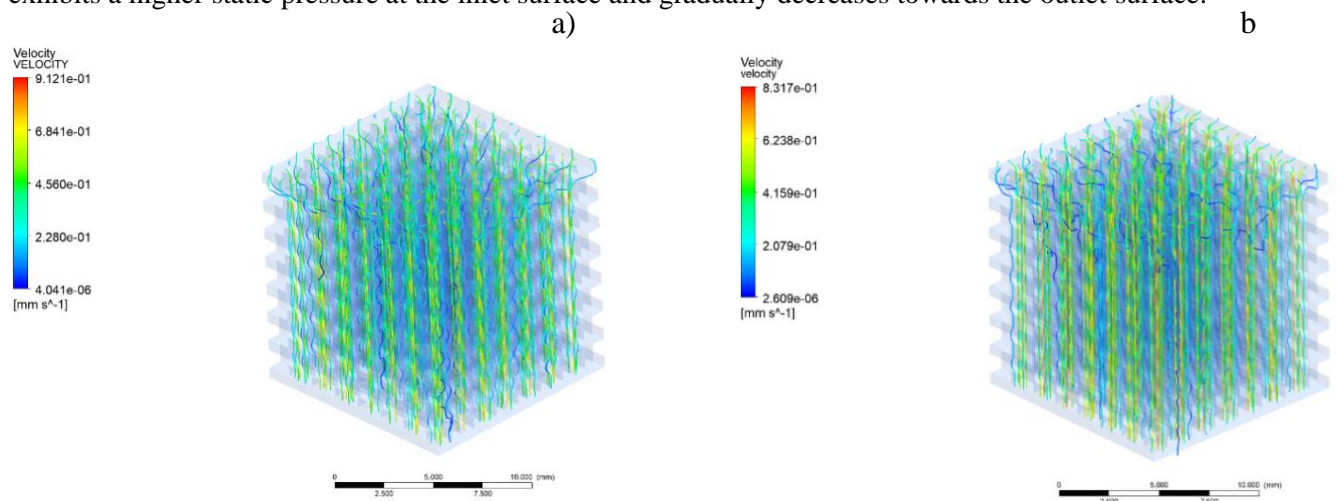


**Fig. 3:** a) Velocity streamline distribution in the scaffold with sharp edges, b) velocity streamline distribution in the scaffold with rounded edges.

The velocity in the inlet surface compared to the outlet surface of the scaffold is higher while the velocity decreases gradually in the radial direction deeper from the central path. The high velocity in the central pathway

indicates the increase in the speed with which it favors cell migration and functional cells to move to the inner region of the scaffold. The gradual decrease in velocity towards the inner boundary is favorable for the absorption of cells and nutrients on the inner surface of the scaffold. The scaffold with the rounded edges presented lower velocity value for all the mesh sizes, which according to Deng et. al. [2] will promote cell adhesion and bone regeneration [7, 8].

#### 4. Conclusions

In this paper, the effect of the scaffold geometry on the osteogenic properties of a scaffold was studied by testing the geometry of the scaffolds. CFD was used to simulate the pressure and velocity in two structures and the internal fluid flow lines to explore the mechanism of the influence of scaffold geometry on bone growth.

The main conclusions are as follows the fluid flow inside the scaffold structure influences on bone tissue growth. Under the same circumstances, the smaller the fluid velocity difference inside the scaffold structure is, the larger the fluid flow area is, the better the bone tissue growth will be. The pressure gradually decreases from the inlet to the outlet. For the two geometries, the pressure is uniformly distributed within the scaffold. The geometry with rounded edges has a lower internal flow rate, and lower velocity (for all mesh sizes), probably allowing cells to attach more easily to the surface of the scaffold, thus promoting bone growth.

#### Acknowledgements

This work is supported by the BIOBON3D project that has received funding from the Operational Programme EPAnEK 2014-2020 and is co-financed by Greece and the Euro-pean Union.

#### References

1. A. K. Abraham, V. M. Biju, S. Suresh, S. Vt, and G. Kg, ‘Computational Fluid Dynamic Analysis and Mechanical Strength Evaluation of Additive Manufactured Customized Bone Scaffolds’, vol. 06, no. 05, p. 7, 2019.
2. F. Deng, L. Liu, Z. Li, and J. Liu, ‘3D printed Ti6Al4V bone scaffolds with different pore structure effects on bone ingrowth’, *J. Biol. Eng.*, vol. 15, no. 1, p. 4, Dec. 2021, doi: 10.1186/s13036-021-00255-8.
3. H. Chen *et al.*, ‘Design and properties of biomimetic irregular scaffolds for bone tissue engineering’, *Comput. Biol. Med.*, vol. 130, p. 104241, Mar. 2021, doi: 10.1016/j.compbimed.2021.104241.
4. S. Zhang, S. Vijayavenkataraman, W. F. Lu, and J. Y. H. Fuh, ‘A review on the use of computational methods to characterize, design, and optimize tissue engineering scaffolds, with a potential in 3D printing fabrication’, *J. Biomed. Mater. Res. B Appl. Biomater.*, vol. 107, no. 5, pp. 1329–1351, Jul. 2019, doi: 10.1002/jbm.b.34226.
5. J. M. Williams *et al.*, ‘Bone tissue engineering using polycaprolactone scaffolds fabricated via selective laser sintering’, *Biomaterials*, vol. 26, no. 23, pp. 4817–4827, Aug. 2005, doi: 10.1016/j.biomaterials.2004.11.057.
6. N. Jusoh *et al.*, ‘CFD Simulation on Permeability of Porous Scaffolds for Human Skeletal System’, *J. Hum. Centered Technol.*, vol. 1, no. 1, pp. 39–47, Feb. 2022, doi: 10.11113/humentech.v1n1.11.
7. D. Ali and S. Sen, ‘Computational Fluid Dynamics Study of the Effects of Surface Roughness on Permeability and Fluid Flow-Induced Wall Shear Stress in Scaffolds’, *Ann. Biomed. Eng.*, vol. 46, no. 12, pp. 2023–2035, Dec. 2018, doi: 10.1007/s10439-018-2101-z.
8. A. B. Kakarla, I. Kong, S. G. Nukala, and W. Kong, ‘Mechanical Behaviour Evaluation of Porous Scaffold for Tissue-Engineering Applications Using Finite Element Analysis’, *J. Compos. Sci.*, vol. 6, no. 2, p. 46, Feb. 2022, doi: 10.3390/jcs6020046.

# Wearable Smart Sensor Patch for Monitoring Knee Laxity

Karthika Sheeja Prakash\*, Vicky Chantal von Einem, Sabari Kannan Muthulagu, Priyank Agarwal, Armin Jamali, Peter Woias, Laura Maria Comella  
Department of Microsystems Engineering – IMTEK, University of Freiburg, Germany  
karthikasprakash@gmail.com\*

## Abstract

The knee joint instabilities caused due to sudden movements of the knee like changing direction, jumping, or landing in an awkward position are prevalent events among youth. Therefore, it is important to have an effective diagnosis for post-injury treatment and recovery for such knee ligament ruptures. Current physical diagnosis methods rely a lot on the examination methods of the examiner and the results vary with each doctor. Also, the current instrumental methods are bulky, non-reproducible, and expensive. These instruments are not ergonomic making it uncomfortable for both the patient and the doctors to carry out effective diagnosis. Therefore, in this paper, a flexible capacitive-based strain sensor that can be worn as a patch is developed for anterior cruciate ligament rupture analysis and is tested for its reliability. The whole system consists of a sensor attached to an electronic board for data acquisition, processing, and wireless transmission. Low-power software and hardware design guarantee the use of the device for several days without recharging. Initial measurements are made with a bench instrument for characterization and testing.

**Keywords:** Strain gauge, microcontroller, low power electronic, wearable sensors, ACL rupture diagnosis

## 1. Introduction

The Anterior Cruciate Ligament (ACL) tear is one of the most common knee injuries. In the physical examination methods, the repeatability and reliability of the measurements is relying on the experience of the physician.[1] Also, the current instrumental diagnosis methods are bulky making the patient uncomfortable during diagnosis and the results are not reproducible.[2, 3] Therefore, a reliable diagnosis method that gives reproducible measurements and satisfies the ergonomic factor is important to attain [4] and is still a challenge in the present day. Therefore, a wearable sensor platform in the form of a smart patch has been developed. The smart patch consists of a flexible capacitive strain gauge sensor [5, 6] optimized for this application and a low-power electronic unit for signal acquisition, data processing, and wireless communication. One of the main challenges for sensor production is the reproducibility of the sensor and for this purpose, it is relevant to have a reliable fabrication method that is cost-effective and easy to implement. In [6], an innovative approach is introduced using the mold fabrication method to obtain several sensors made in batches with a high reproducibility rate, and the same is achieved. In this smart sensor system, the sensors produced by this innovative approach are utilized. [6] The flexible patch in which all necessary components are integrated without compromising the desired high elasticity of the sensor elements. Production methods were developed for the integration of stretchable sensors and flexible electronics by making them fully adherent to the skin. Moreover, an attentive analysis of the material and its behavior has been done to obtain reliable measurements providing for full biocompatibility and medical compliance of the platform. The result is a flexible and ergonomic platform, which can be used for diagnosis in the clinic. This has been first tested in the lab for reliability and functionality check. As a result, a knee robot was used to simulate the leg movements of a real patient. Moreover, the design of low-power software and electronics permits a long battery life. To make the system suitable for clinical use, the device must be (1) light and wearable, (2) must allow wireless data transfer, and (3) permit a long battery life.

## 2. Capacitive Sensor

### 2.1 Sensor design and fabrication

From the different types of sensors, a stretchable capacitive [7–12] based strain gauge is chosen for the application. The sensing part of the sensor is obtained by adding carbon particles (ENSACO® 250 P from TIMCAL Ltd., Bodio, Switzerland) to the non-conductive polydimethylsiloxane (PDMS). This carbon black layer is laser patterned to the raw substrate layer of PDMS (Neukasil® RTV-23 and RTV-17). A comb-shaped electrode is patterned using the Nd: YAG laser with a wavelength of 1064 nm (DPL Smart Marker II, ACI Laser

GmbH, Nohra, Germany) and has 279 fingers. The sensor is subjected to batch fabrication where at least 5 sensors can be produced from a single fabrication. The sensors obtained are reproducible and achieve a repeatable and reliable measurement. [6] The fabricated sensor is further connected to the electronics for data transmission. The sensor structure is as shown in Fig. 1 [6] with the dimensions in mm.



Fig. 1: Capacitive strain gauge sensor. [6]

## 2.2 Electronic System

The microcontroller CC2652R1 (Texas Instruments) was chosen, the properties of which satisfy the system requirements. (1) The ultra-low-power microcontroller unit (MCU) consumes 3.39 mA in the active state and is at standby at 3.2  $\mu$ A (2) It features autonomous data acquisition without the main CPU. (3) Ultra-low energy consumption for the sensor controller unit – Active mode: 808.5  $\mu$ A and Low-power mode: 30.1  $\mu$ A (4) In the chip is integrated a time to digital converter for capacitive sensing, and a Bluetooth low-energy unit. Further, the main feature of the MCU to save energy is utilized by programming to a mode that the MCU shuts down the main Central Processing Unit (CPU) and lets the periphery work. When the data is ready, an alert from the sensor controller to the main CPU is given and then the CPU wakes up to copy the data from the buffer to the main random-access memory (RAM). After this process, the CPU releases the buffer. The radio frequency (RF core) sends a notification that 10 measurement data are sent in one package at a frequency of 200 Hz. At the receiver end, a BLE 112 USB dongle (Silicon labs) is used for the data gathering. Bluetooth 4.0 (low energy) is adapted and the communication is via the virtual COM port. The dongle is connected to the computer where the data is recorded using MATLAB software.

## 3. Measurement Principle

The CC2652R1 microcontroller has the time to digital (TDC) converter integrated into it. The real-time clock of the microcontroller counts the time taken to charge the capacitor and the current consumed for the same is 4.5  $\mu$ A. Therefore, the CC2652R1 shows clock ticks or clock periods as a function of the capacitance.

## 4. Measurement Setup

A knee simulator developed in [4] is used to mimic the movements of an actual leg. The knee simulator consists of an X-Y rotary table (Intel Li Drives Inc., Philadelphia, PA, USA), and three NEMA17 motors to drive the table. The flexion and extension movements are made possible with the spindle motor NEMA23. The whole setup is controlled with 2D interactive software (NI MAX - Measurement &Automation Explorer). The

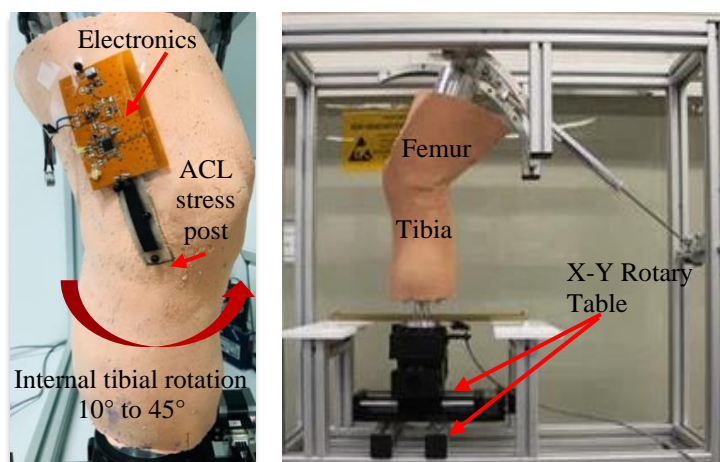


Fig. 2: Knee simulator setup

capacitive strain gauge sensor is contacted to the electronic board using small metal screws. The attachment of the sensor to the electronic board [13] is shown in Fig. 2. The measurement method involves analysis of the rotation movement of the knee to a corresponding angle at a certain speed. This would be the same course of action that would be performed by a physician in a clinical test to analyze the knee joint instabilities. In the real scenario, the clinicians use a laxitester to measure the rotational laxity of the knee joint. The sensor and the electronics are subjected to knee rotation of  $5^{\circ}$  to  $45^{\circ}$  which qualifies as the maximum and minimum angle of rotation that is possible with an actual knee using the laxitester as per the doctor’s analysis. This angle varies from patient to patient depending on the stretchability of the ligament tissue. A force of 200 N max is applied to rotate the knee and the corresponding angle in the scale of the laxitester is noted. [13, 14]. The knee simulator is rotated between  $5^{\circ}$  to  $45^{\circ}$  with a  $5^{\circ}$  interval.

### 5. Result and Discussion

The capacitive strain sensor placed on the ACL stress post of the knee simulator is stretched 3 times in different cycles of rotation. In each rotation, the sensor undergoes an elastic strain that directly translates to the number of clock ticks. These clock ticks are then converted to capacitance. The relative capacitance data of 3 cycles of rotation is compared with the second-order polynomial equation for fitting. As a result, it has a good correspondence as the R-square value is 0.99946 which is close to 1. The data plot and equation data are shown in Fig.3 and Table 1 below:

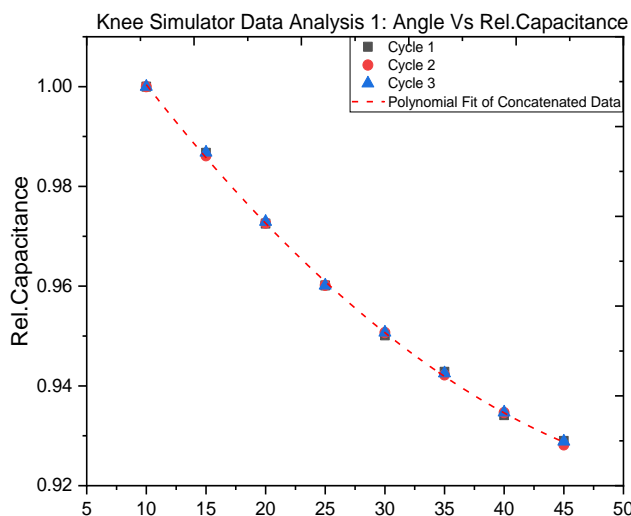


Fig.3 : Knee simulator data analysis

Table 1: Second-order polynomial fit parameter values

Equation	$y = \text{Intercept} + B1*x^1 + B2*x^2$
Plot	Concatenated Data
Weight	No Weighting
Intercept	$1.03401 \pm 6.95183E-4$
B1	$-0.00365 \pm 5.61289E-5$
B2	$2.92183E-5 \pm 1.00406E-6$
Residual Sum of Squares	6.66888E-6
R-Square (COD)	0.99951
Adj. R-Square	0.99946

Furthermore, a comparative study between the human leg and the knee simulator data could be executed to further validate the measurement setup. One of the main advantages is that after passing the initial tests on healthy voluntary subjects, it can also be worn by patients with knee joint instabilities in everyday life for continuous observation and monitoring of the ACL tear over an extended time, to gain a better understanding of pathology and methods to cure it.

### Acknowledgment

The German Science Foundation (DFG) is acknowledged for funding this project (grant number: 222567169, and internal DFG funding number: WO 883/16 3).

### References

- [1] T. P. Branch, H. O. Mayr, J. E. Browne, J. C. Campbell, A. Stoehr, and C. A. Jacobs, “Instrumented examination of anterior cruciate ligament injuries: minimizing flaws of the manual clinical examination,” *Arthroscopy : the journal of arthroscopic & related surgery : official publication of the Arthroscopy Association of North America and the International Arthroscopy Association*, vol. 26, no. 7, pp. 997–1004, 2010, doi: 10.1016/j.arthro.2010.01.019.
- [2] H. O. Mayr and A. Stöhr, *Aktueller Stand der instrumentellen Messung der Knielaxität. Arthroskopie* 23(1):56-61, 2010.
- [3] M. Ahldén, K. Samuelsson, F. H Fu, V. Musahl, and J. Karlsson, “Rotatory Knee Laxity,” *Clinics in Sports Medicine*, vol. 32, no. 1, pp. 37–46, Jan. 2013, doi: 10.1016/j.csm.2012.08.005.
- [4] M. Zens *et al.*, “Novel approach to dynamic knee laxity measurement using capacitive strain gauges,” *Knee Surg Sports Traumatol Arthrosc*, vol. 23, no. 10, pp. 2868–2875, 2015, doi: 10.1109/MeMeA.2014.6860064.
- [5] M. Zens, “Kapazitive Polydimethylsiloxansensoren für biomechanische Anwendungen, Master Thesis,” Technical University of Freiburg, Freiburg, Germany, 21 March/2016. [Online]. Available: [https://www.researchgate.net/publication/308959523\\_Kapazitive\\_Polydimethylsiloxansensoren\\_fur\\_biomechanische\\_Anwendungen](https://www.researchgate.net/publication/308959523_Kapazitive_Polydimethylsiloxansensoren_fur_biomechanische_Anwendungen)
- [6] K. Sheeja Prakash *et al.*, “Batch Fabrication of a Polydimethylsiloxane Based Stretchable Capacitive Strain Gauge Sensor for Orthopedics,” *Polymers*, vol. 14, no. 12, 2022, doi: 10.3390/polym14122326.
- [7] W. A. D. M. Jayathilaka *et al.*, “Significance of Nanomaterials in Wearables: A Review on Wearable Actuators and Sensors,” *Adv. Mater.*, vol. 31, no. 7, e1805921, 2019, doi: 10.1002/adma.201805921.
- [8] J. Li, L. Fang, B. Sun, X. Li, and S. H. Kang, “Review—Recent Progress in Flexible and Stretchable Piezoresistive Sensors and Their Applications,” *J. Electrochem. Soc.*, vol. 167, no. 3, p. 37561, 2020, doi: 10.1149/1945-7111/ab6828.
- [9] H. Souri *et al.*, “Wearable and Stretchable Strain Sensors: Materials, Sensing Mechanisms, and Applications,” *Advanced Intelligent Systems*, vol. 2, no. 8, p. 2000039, 2020, doi: 10.1002/aisy.202000039.
- [10] J. Shintake, T. Nagai, and K. Ogishima, “Sensitivity Improvement of Highly Stretchable Capacitive Strain Sensors by Hierarchical Auxetic Structures,” *Frontiers in robotics and AI*, vol. 6, p. 127, 2019, doi: 10.3389/frobt.2019.00127.

- [11] J. Shintake, Y. Piskarev, S. H. Jeong, and D. Floreano, “Ultrastretchable Strain Sensors Using Carbon Black-Filled Elastomer Composites and Comparison of Capacitive Versus Resistive Sensors,” *Adv. Mater. Technol.*, vol. 3, no. 3, p. 1700284, 2018, doi: 10.1002/admt.201700284.
- [12] M. Amjadi, K.-U. Kyung, I. Park, and M. Sitti, “Stretchable, Skin-Mountable, and Wearable Strain Sensors and Their Potential Applications: A Review,” *Adv. Funct. Mater.*, vol. 26, no. 11, pp. 1678–1698, 2016, doi: 10.1002/adfm.201504755.
- [13] H. O. Mayr *et al.*, “Validation of a measurement device for instrumented quantification of anterior translation and rotational assessment of the knee,” *Arthroscopy : the journal of arthroscopic & related surgery : official publication of the Arthroscopy Association of North America and the International Arthroscopy Association*, vol. 27, no. 8, pp. 1096–1104, 2011, doi: 10.1016/j.arthro.2011.02.034.
- [14] H. O. Mayr *et al.*, “Rotational laxity and collateral ligament laxity following total knee arthroplasty with rotating platform,” *International Orthopaedics*, vol. 38, no. 7, pp. 1379–1386, 2014, doi: 10.1007/s00264-014-2308-z.

# Hydrophobic coating encompassing visibility-on-demand for smart and rapid quality control

C.Bandl<sup>1</sup>, W. Kern<sup>1</sup>, M. Müller<sup>1</sup>, N. Kremp<sup>2</sup>, M. Kratzer<sup>3</sup>

<sup>1</sup>Montanuniversität Leoben, Chair in Chemistry of Polymeric Materials  
Otto-Glöckel-Straße 2, 8700 Leoben – Austria, [Christine.bandl@unileoben.ac.at](mailto:Christine.bandl@unileoben.ac.at)

<sup>2</sup>Montanuniversität Leoben, Chair in Polymer Processing  
Otto-Glöckel-Straße 2, A-8700 Leoben – Austria

<sup>3</sup>Montanuniversität Leoben, Chair in Physics  
Franz-Josef-Straße 18, 8700 Leoben, Austria

## Abstract

There is a wide application field for hydrophobic coatings ranging from self-cleaning surfaces over anti-graffiti coatings, separation layers for adhesive tapes and labels to demolding aids in the production of polymers. In our previous studies we developed an anti-adhesive coating based on perfluorinated organosilanes, which was extended by a visibility-on-demand property enabling temporary quality control in the present work. For this purpose, 1,8-naphthalimide-N-propyltriethoxysilane (NIPTES) was synthesized and deposited together with the silanes of the anti-adhesive formulation in a sol-gel process (hydrolysis and condensation).

The coated substrates were investigated with regard to their surface energy by contact angle measurements, while different spectroscopic techniques such as XPS, FTIR, UV-Vis and fluorescence spectroscopy were used to study their surface composition and optical properties. Furthermore, the adhesion force of the coating was determined using AFM. The on-demand control function of the coating was examined by means of injection molding experiments, monitoring the abrasion and wear of the coating along repeated injection molding cycles. It was shown that the incorporation of NIPTES as a fluorescent marker represents a straightforward and temporary approach for quality control of the applied anti-adhesive coating.

**Keywords:** hydrophobic, anti-adhesive, coating, fluorescence, organosilane, visibility-on-demand, naphthalimide

## 1. Introduction

Organosilanes are well known for their application as surface modifiers, coupling agents [1], [2] and protective layers [3], [4]. Based on their bifunctional structure, they are able to interact and undergo chemical reactions with both organic and inorganic materials employing their organofunctional moieties and hydrolyzable groups, respectively [1]. Coupling to inorganic surfaces is achieved via a series of hydrolysis and condensation reactions [5] Simultaneously, a polysiloxane network is built at the surface [1], [2], [6]–[8].

In general, coatings and damages of the same can be detected by various characterization methods such as (i) microscopy (SEM, AFM, etc.), (ii) spectroscopy (XPS, FT-IR) and (iii) interferometry. [9] Moreover, profilometry, contact angle measurements, ultrasonic inspection, acoustic emission and radiography can be employed. However, these techniques are time consuming, costly, require bulky equipment and an external energy supply, and are often very complex, which makes them impractical for the detection over large areas and also unsuitable for application in industrial processes. Alternatively, fluorescent, colour changing or mechanically triggered indicators can be incorporated into coatings. [10] The use of fluorescent markers (e.g. coumarins, naphthalimides, fluorescein, BODIPY dyes [11]–[13] the green fluorescent protein (GFP) [13]–[17]) is already well-established in biomedical applications such as the localization of biomolecules and the examination of biological processes [14], [18], [19] as well as in the discovery of new drugs, environmental analysis and medical applications (e.g. detection of cancer) [11]. Moreover, organosilanes comprising fluorescent moieties are employed as optical markers in more technical applications including the control of the uniformity of polymer layers [20], investigation of interfaces [21], [22] and the detection of explosives and pesticides [23]. Also, the inherent fluorescence of selected polymer matrices was utilized for the optical detection of inhomogeneities, cracks and other defects. [24]

In this work, the concept of fluorescence labeling is transferred to the field of low surface energy coatings by extending an already established anti-adhesive layer by a visibility-on-demand property, representing a quick

and straightforward approach to temporarily monitor the presence and homogeneity of the applied organosilane layer.

## 2. Results and Discussion

The silane-based marker 1,8-naphthalimide-N-propyltriethoxysilane (NIPTES) was synthesized and deposited together with a fluoroalkyl and a dipodal organosilane of the anti-adhesive coating (see Figure 1) in a sol gel process. The ethoxy groups in NIPTES enable covalent coupling to the coating as a consequence of hydrolysis and condensation reactions, while the naphthalimide unit provides blue fluorescence under UV-irradiation.

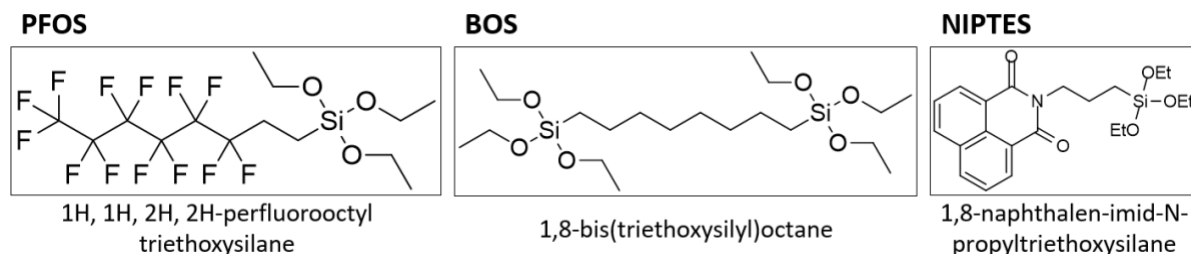


**Figure 1:** Chemical structures of the applied organosilanes PFOS, BOS and NIPTES

Organosilane coatings were prepared on Si wafers and steel substrates via drop casting and brush coating, respectively. More details about sample preparation and methods can be found in Ref [25].

Successful incorporation of NIPTES into the anti-adhesive coating was proven by FTIR and XPS spectroscopy. More precisely, the peak at 1590-1710  $\text{cm}^{-1}$  was assigned to the  $\text{-C=O}$  moieties of the imide bond in NIPTES and was only found in the IR spectra of organosilane layers containing this fluorescent marker (see Figure 2a). In addition, XPS revealed that N was exclusively detected for coatings with incorporated fluorescent marker (see Figure 2b) since it originates from the imide moiety of NIPTES.

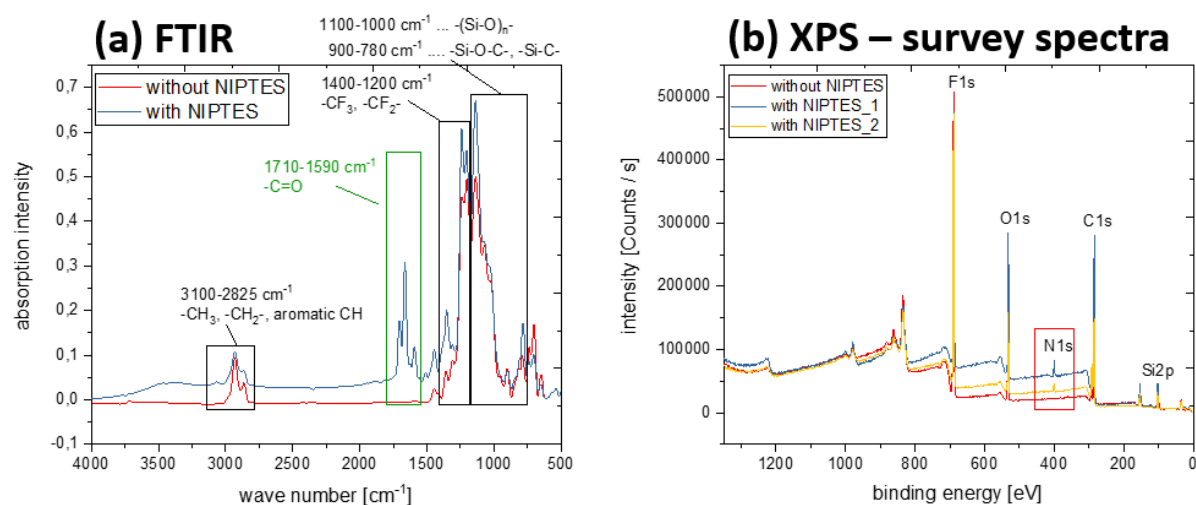


**Figure 2:** FTIR and XPS spectra of the basic coating (without NIPTES and NIPTES containing coatings)

Moreover, the absorption and emission properties of NIPTES containing coatings were investigated by UV-Vis and fluorescence spectroscopy. The results showed that NIPTES is suitable to absorb UV light in the range of 220-240 nm as well as 310-370 nm and to emit blue fluorescence with an emission maximum at 461 nm as a consequence of UV absorption.

Finally, application related properties of the coating were investigated. Adhesion force measurements using AFM and water contact angle (WCA) measurements proved that the anti-adhesive effect of the basic coating (without NIPTES) was still maintained after incorporation of the fluorescent marker. As shown in Table 1, the adhesion forces of the basic and the fluorescent coatings are at the same scale (0.16-0.25  $\text{nN}/\text{nm}^2$ ) and are significantly lower compared to the uncoated steel substrate ( $2.35 \pm 0.77 \text{ nN}/\text{nm}^2$ ). Moreover, the high WCA

of the basic and fluorescent coatings (107-116 °) indicate low surface energy, which is related to the anti-adhesive effect of fluorinated polymer surfaces. [26][25]

**Table 1:** normalized adhesion force of uncoated and coated steel substrates

sample	Normalized adhesion force [nN/nm <sup>2</sup> ]	Water contact angle [°]
Uncoated Ref	2.35 ± 0.77	60.3 ± 3.9
Coating without NIPTES	0.25 ± 0.08	116.1 ± 2.8
Coating with NIPTES_1	0.16 ± 0.02	107.1 ± 0.9
Coating with NIPTES_2	0.19 ± 0.02	112.4 ± 1.4

In addition, injection experiments were performed with chalk filled polypropylene, causing abrasion of the coating over repeated injection molding cycles. By the use of a UV lamp, the wear of the fluorescent coating was controlled easily (see Figure 3), fulfilling the requirements of an on-demand quality control.



**Figure 3:** NIPTES containing coating along injection molding experiment

#### 4. Conclusion

The incorporation of NIPTES into the basic organosilane coating was proven by FTIR and XPS measurements. UV-Vis and fluorescence spectroscopy showed that NIPTES is a suitable fluorescent marker, which absorbs UV light and emits blue fluorescence. Adhesion force and WCA measurements evidenced that the anti-adhesive effect of the basic coating was still maintained after incorporation of NIPTES. The proposed on-demand quality control function of the fluorescent coating was demonstrated in injection molding experiments, in which abrasion was followed along repeated injection molding cycles. Advantages of this method are (i) the simple, quick and temporary approach using a conventional UV lamp to access information about the presence, homogeneity and damage of the applied coating, (ii) the fact that the complete coated area can be controlled instead of testing small representative spots on the sample surface and (iii) the direct integration of NIPTES into the coating using the same organosilane chemistry, which avoids additional preparation steps.

#### Acknowledgements

Thanks go to Dr. Georg Jakopic from Joanneum Research Materials (Weiz, Austria) for performing the ellipsometric measurements and profilometry. Matthias Müller wishes to thank Montanuniversitaet Leoben for funding his PhD thesis within a special program.

#### References

1. E. P. Plueddemann, *Silane Coupling Agents*, 1st ed. Springer Science+Business Media, LLC, 1982.
2. K. L. Mittal, Ed., *Silanes and Other Coupling Agents*, 5th ed. Leiden, Boston: CRC Press Taylor & Francis Group, 2009.
3. X. Fu and X. He, "Fabrication of super-hydrophobic surfaces on aluminum alloy substrates," *Appl. Surf. Sci.*, vol. 255, pp. 1776–1781, 2008.
4. J. Brassard, D. K. Sarkar, and J. Perron, "Fluorine Based Superhydrophobic Coatings," *Appl. Sci.*, vol. 2, pp. 453–464, 2012.
5. S. Zheng and J. Li, "Inorganic-organic sol gel hybrid coatings for corrosion protection of metals," *J. Sol-Gel Sci. Technol.*, vol. 54, no. 2, pp. 174–187, 2010.
6. W. Brockmann, P. Ludwig Geiß, J. Klengen, and S. Bernhard, *Adhesive Bonding Materials, Applications and Technology*, vol. 1. Weinheim: WILEY-VCH Verlag GmbH & Co KGaA, 2009.
7. A. V. Pocius, *Adhesion and Adhesives Technology - An Introduction*, 3rd ed. Munich: Carl Hanser Verlag, 2012.
8. G. Habenicht, *Kleben: Grundlagen, Technologien, Anwendungen*, 6th ed. Berlin, Heidelberg: Springer Verlag Berlin

- Heidelberg, 2009.
9. X. Feng, N. Senin, R. Su, S. Ramasamy, and R. Leach, “Optical measurement of surface topographies with transparent coatings,” *Opt. Lasers Eng.*, vol. 121, no. 800, pp. 261–270, 2019.
  10. L. Ma *et al.*, “Self-reporting coatings for autonomous detection of coating damage and metal corrosion: A review,” *Chem. Eng. J.*, vol. 421, no. P2, p. 127854, 2021.
  11. Y. Fu and N. S. Finney, “Small-molecule fluorescent probes and their design,” *RSC Adv.*, vol. 8, no. 51, pp. 29051–29061, 2018.
  12. M. Y. Berezin and S. Achilefu, “Fluorescence lifetime measurements and biological imaging,” *Chem. Rev.*, vol. 110, no. 5, pp. 2641–2684, 2010.
  13. H. Kobayashi, M. Ogawa, R. Alford, P. L. Choyke, and Y. Urano, “New Strategies for Fluorescent Probe Design in Medical Diagnostic Imaging,” *Chem. rev.*, vol. 110, pp. 2620–2640, 2010.
  14. J. Liu, J. Liu, Z. Cui, and Z. Cui, “Fluorescent Labeling of Proteins of Interest in Live Cells: Beyond Fluorescent Proteins,” *Bioconjug. Chem.*, vol. 31, no. 6, pp. 1587–1595, 2020.
  15. K. Nienhaus and G. Ulrich Nienhaus, “Fluorescent proteins for live-cell imaging with super-resolution,” *Chem. Soc. Rev.*, vol. 43, no. 4, pp. 1088–1106, 2014.
  16. J. Lippincott-Schwartz and G. H. Patterson, “Development and use of fluorescent protein markers in living cells,” *Science (80-. )*, vol. 300, no. 5616, pp. 87–91, 2003.
  17. R. N. Day and M. W. Davidson, “The fluorescent protein palette: Tools for cellular imaging,” *Chem. Soc. Rev.*, vol. 38, no. 10, pp. 2887–2921, 2009.
  18. C. P. Toseland, “Fluorescent labeling and modification of proteins,” *J. Chem. Biol.*, vol. 6, no. 3, pp. 85–95, 2013.
  19. N. Fili and C. P. Toseland, “Fluorescence and labelling: how to choose and what to do,” in *Fluorescent Methods for Molecular Motors*, C. Toseland and N. Fili, Eds. Springer, Basel, 2014, pp. 1–24.
  20. S. D. Conzone, A. Burzio, and D. Haines, “Non-destructive quality control method for microarray substrate coatings via labeled doping,” US 2004/0258927 A1, 2004.
  21. J. L. Lenhart, J. P. Dunkers, J. H. Van Zanten, and R. S. Parnas, “Characterization of sizing layers and buried polymer/sizing/substrate interfacial regions using a localized fluorescent probe,” *J. Colloid Interface Sci.*, vol. 257, no. 2, pp. 398–407, 2003.
  22. J. L. Lenhart, J. H. Van Zanten, J. P. Dunkers, and R. S. Parnas, “Using a localized fluorescent dye to probe the glass/resin interphase,” *Polym. Compos.*, vol. 23, no. 4, pp. 555–563, 2002.
  23. K. Rurack and M. Biyikal, “Fluorescent Silane Layers for detecting explosives.pdf,” WO 2018/153922 A1, 2018.
  24. M. F. D’Elia, M. Magni, S. P. M. Trasatti, T. B. Schweizer, M. Niederberger, and W. Caseri, “Poly(phenylene methylene)-based coatings for corrosion protection: Replacement of additives by use of copolymers,” *Appl. Sci.*, vol. 9, no. 17, pp. 1–14, 2019.
  25. W. Kern, M. Müller, C. Bandl, N. Krempl, and M. Kratzer, “Anti-Adhesive Organosilane Coating Comprising Visibility on Demand,” *Polymers (Basel)*, vol. 14, no. 19, 2022.
  26. C. Bandl, W. Kern, N. Krempl, and W. Friesenbichler, “Simple and rapid method for restoring anti-adhesive organosilane coatings on metal substrates,” *Prog. Org. Coatings*, vol. 140, pp. 105490–105500, 2020.

# Graphene Field Effect Transistor gas sensors

Abdullah K. Aladim<sup>1</sup>, Toby Hallam<sup>1</sup>

<sup>1</sup>School of Mathematics Statistics and Physics, Newcastle University, Newcastle-Upon-Tyne  
abdulh.k@ju.edu.sa

## Abstract

Electrical tunability of molecular adsorption on graphene has been studied using a back gate Field Effect Transistor (GFET). Changing the gate voltage from positive to negative voltage values results in shifting the Dirac point toward positive voltage as the p-type doping of NO<sub>2</sub> increases. The reverse behaviour was observed for the n-typed doping by NH<sub>3</sub>. The charge doping density increases as the concentration of the oxidising gases increase (NO<sub>2</sub>). At the same time, the opposite was observed for reducing gas (NH<sub>3</sub>). The conductivity change with molecular adsorption as the NO<sub>2</sub> increase the conductivity while NH<sub>3</sub> decrease it. Exposure of GFETs to different gaseous environments demonstrates that the sensor can distinguish gases, such as NO<sub>2</sub> and NH<sub>3</sub>, as the Dirac point shift toward positive voltage with NO<sub>2</sub> and toward negative voltage with NH<sub>3</sub>.

**Keywords:** 2D material, GFET gas sensors, Gas sensors, resistive sensors.

## 1. Introduction

Graphene has attracted the attention of researchers due to its high surface to volume ratio, conductivity, electric mobility, absorption ability, and low density of states near the Dirac point [1-3]. Graphene can operate as a gas sensor at room temperature which results in low energy consumption in comparison to other key sensing technologies [4].

Graphene is well suited to use within gas sensing devices, due to its ultimately large surface-to-volume ratio [1] and thinness [2]. In particular, graphene's atomic thickness means that any adsorbate on the graphene will have the effect of doping the entire graphene channel thickness [1, 5]. In addition, graphene typically presents charge carrier mobilities in excess of 1000 cm<sup>2</sup>/(V.s), even for poorly prepared samples, whilst also possessing a low density of states close to its Dirac point [3]. Taken in combination, these factors make graphene an ideal candidate for gas sensing, as even modest charge exchange interactions between the graphene sheet and adsorbates should produce a measurable change in the graphene's conductivity [6, 7] and shift in the Dirac point of the graphene channel [6-8].

The conductivity of graphene is influenced by the analyt, molecules, for instance, NO<sub>2</sub> and NH<sub>3</sub> as an electron acceptor and downer respectively [6-10]. Additionally, chemical vapor deposition (CVD) graphene (G) demonstrates strong p-type nature of the graphene film. Also, the mobility depends on a cleanliness of graphene field effect transistor (GFET). Therefore the cleaner GFETs mean the greater sensitivity [11]. Singh et al. demonstrated NO<sub>2</sub> and NH<sub>3</sub> sensing, at 20ppm and 550ppm respectively, using GFETs with a mobility of 10.15 cm<sup>2</sup>/V.s [5]. Two different measurement regimes are used to determine the sensitivity of the device – one regime involves sweeping back gate voltage and monitoring the change of Dirac point and the second regime is carried out by modulation via back gate bias and then measure channel conductivity [6]. In separate study, Wei et al. demonstrated detection limit of nitrogen dioxide (NO<sub>2</sub>) and ammonia (NH<sub>3</sub>) in ambient conditions [7]. The GFET mobility for the sensor was 1304 cm<sup>2</sup>/V.s. Moreover, their device limit of sensitivity detection to NO<sub>2</sub> and NH<sub>3</sub> was found to be 50ppm. Other publication shows that GFETs can detect 0.1ppm and 0.5ppm of NO<sub>2</sub> and NH<sub>3</sub> respectively at room temperature [8]. Researchers [8, 9] show GFETs with mobility of 500 to 3000 cm<sup>2</sup>/V.s can detect NO<sub>2</sub> and NH<sub>3</sub>. Blechta et al [3] demonstrated detection of NO<sub>2</sub> at 2ppm using GFET devices with charge carrier mobilities of 1100 cm<sup>2</sup>/V.s.

In this work, we demonstrate that analyt gas can cause a detectable shift in the Dirac point as the adsorption of the gas on the graphene channel causes charge transfer, affecting the charge carrier concentration. The Dirac point will shift either toward positive or negative voltage depending on the increase or decrease of the charge carrier concentration.

## 2. Experimental

In this work, graphene was grown on a copper (Cu) substrate via CVD. After loading the Cu substrate into the CVD reactor, the reactor is heated to 1050°C under a constant flow of 100 sccm of nitrogen (N<sub>2</sub>). Once 1050°C is reached, the copper substrate is annealed for 30 minutes under a flow of 100 sccm of N<sub>2</sub> at 1050°C. Following annealing, 20 sccm of 2% methane/argon (CH<sub>4</sub>) and 1000 sccm of 2% hydrogen/argon (H<sub>2</sub>) were introduced in the chamber for 30 minutes to grow graphene. Finally, the chamber is cooled to below 100°C and the CH<sub>4</sub> and H<sub>2</sub> flow reduced to 200 sccm and 1000sccm respectively during the cooling process.

To transfer the graphene, cellulose nitrate is spin-cast on the graphene to support it during the etching process. Ammonium persulfate solution of 0.5 M was used to etch the copper. After that the graphene sheet rinsed with Deionised water (DI) and transferred to silicon dioxide on silicon (SiO<sub>2</sub>/Si). Finally, the cellulose nitrate (CN) was removed by acetone.

Following CVD, graphene is transferred onto Si substrates, capped with 300 nm SiO<sub>2</sub>. Prior to graphene transfer, the substrates are pre-patterned with Cr/Au (10 nm/60 nm) electrodes via thermal evaporation, as displayed in Figure 1. The displayed configuration provides 11 graphene channels per chip, with the underlying Si acting as a global back gate.

Graphene transfer is achieved via spin casting CN on the graphene/Cu stack, to act as a graphene support during Cu etching. Ammonium persulphate (0.5 M) is then used to etch the copper growth substrate.

Following transfer and CN removal, electric measurement are taken from all channels. The Dirac point for the forward sweep for all the 11 channels (ch1- ch11) ranges between 22-25 V and for the backward sweep range between 5-8V. Transconductance ( $g_m$ ) was calculated by,

$$g_m = \frac{dI_{ds}}{dV}$$

Where:  $dI_{ds}$  is the derivative of the source current and  $dV$  is the derivative of the gate voltage.

Charge carrier mobility can then be calculated by using the gradual channel approximation [12]

$$\mu = \frac{g_m \cdot l}{W \cdot V_{ds} \cdot C}$$

Where:  $l$  is the channel length,  $W$  is the channel width,  $V_{ds}$  is source voltage, and  $C$  is the capacitance.

From the calculation, the average electron and hole mobility was found to be 1180 and 2865  $\text{cm}^2/\text{V}\cdot\text{s}$  respectively.

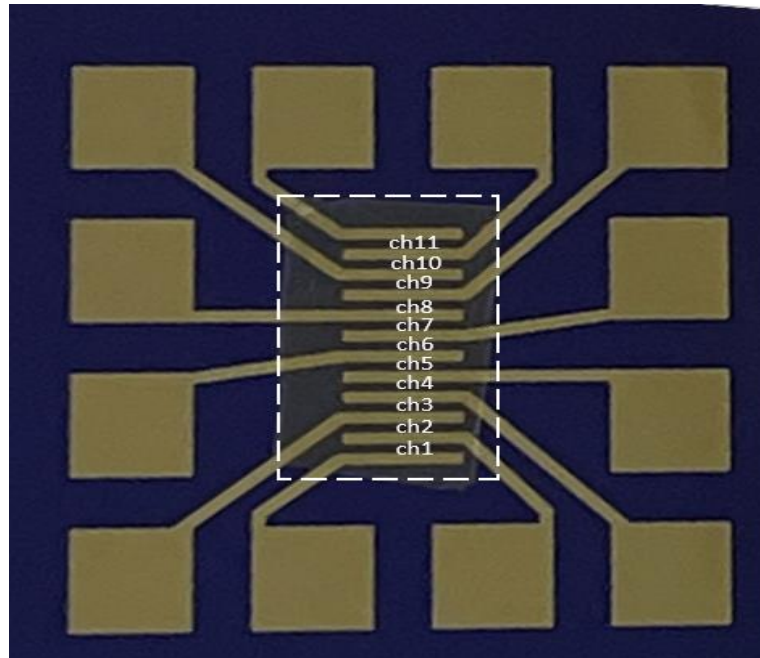


**Fig 1:** shows the device shape after depositing electrode on it and graphene.

## 2.1 Dirac point measurements

In this measurement, we swept the gate voltage from -80V to 80 V at 1mV drain voltage bias and recorded the Dirac point for each channel, with the absence of the test gas. After that, expose the device to 0.1ppm of  $\text{NO}_2$  and record the change in the Dirac point. Then, increase the concentration of the  $\text{NO}_2$  up to 1ppm and record the variation in the Dirac point. Repeat the same process but with  $\text{NH}_3$ . We started with 1ppm of  $\text{NH}_3$  for the first measurement and increased the concentration of  $\text{NH}_3$  for the rest of the measurements up to 10ppm.

### 3. Results and discussion

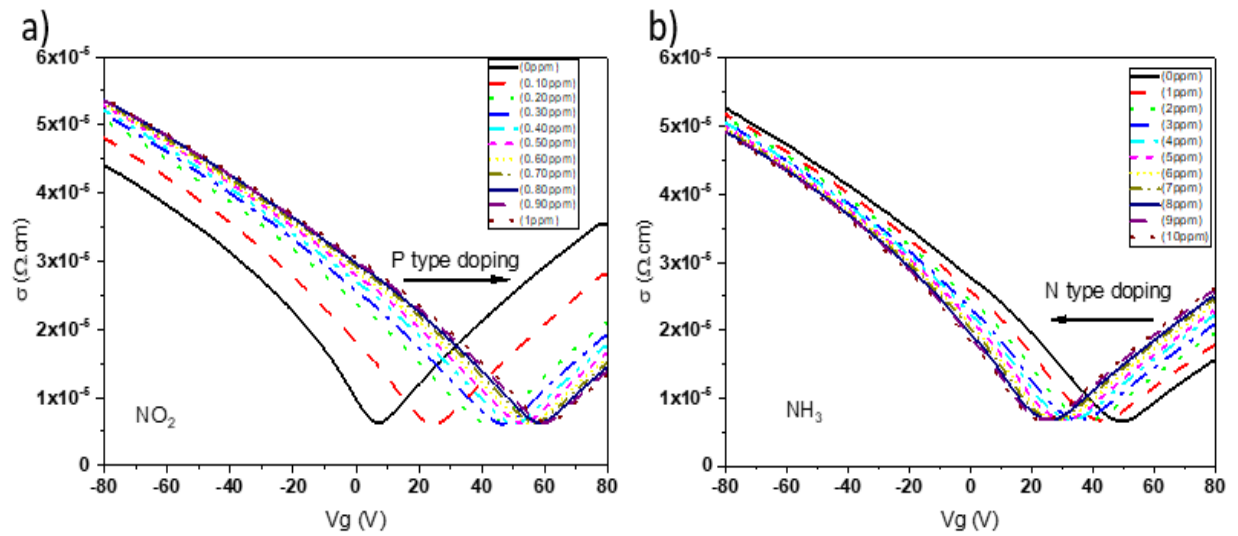


**Fig 2:** represents the change in conductivity and Dirac point shift upon exposure to the different gas concentrations. ( a ) shows the increase in conductivity with respect to exposure to oxidising gas  $\text{NO}_2$  and the Dirac shift toward positive voltage as the concentration increases from 0 to 1ppm. ( b ) shows the opposite behaviour upon exposure to reducing gas  $\text{NH}_3$  by changing the concentration from 0 to 10 ppm.

Gas adsorption on the graphene channel causes an increase in the conductivity as the resistance of GFETs decreases with existing gases, and the opposite happens for the reducing gases. Fig. 2a. shows the shift of the Dirac point toward positive voltage with gas adsorption of  $\text{NO}_2$ . In addition, as the concentration of  $\text{NO}_2$  increases, the Dirac shift toward high positive voltage. Resulting in more decrease in sensors resistance. Fig. 2b. demonstrate the shift of the Dirac point upon exposure to  $\text{NH}_3$ ; as the concentration of  $\text{NH}_3$  increases, the Dirac point shifts more toward negative voltage. The conductivity decreases as the  $\text{NH}_3$  donate an electron to the graphene channel, which depletes the hole charge carrier. Resulting in an upward shift of the Fermi level relative to the Dirac point. Figure. 3a. represents the shift in the Dirac point to high positive voltage with respect to exposure to the gas concentration of  $\text{NO}_2$ . The reverses shift of the Dirac point was observed for  $\text{NH}_3$  exposure. The charge carrier concentration increases with  $\text{NO}_2$  adsorption concentration, as presented in fig. 4a. while decreasing with  $\text{NH}_3$  concentration, as demonstrated in fig. 4b.

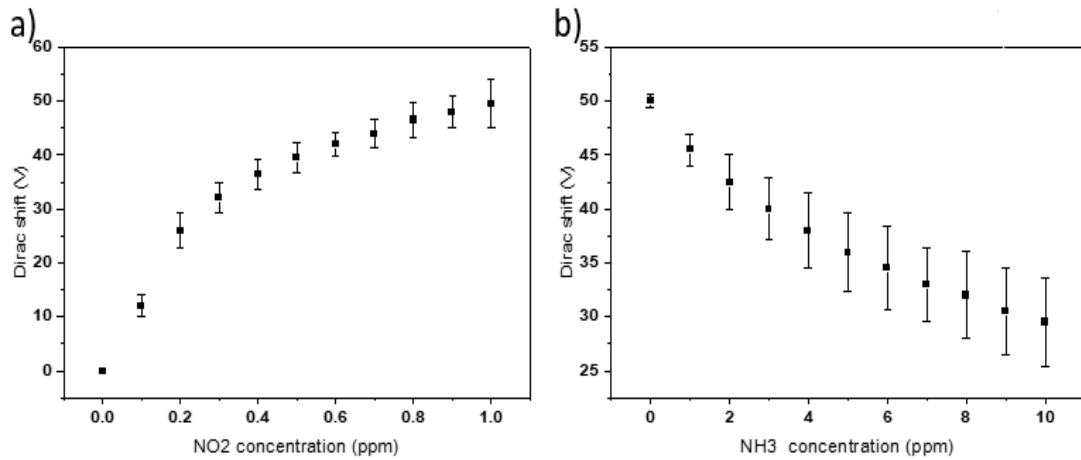


**Fig.3:** (a) shows the shift in Dirac point with changing the NO<sub>2</sub> concentration. (b) represent the shift of the Dirac point with changing NH<sub>3</sub> concentration.

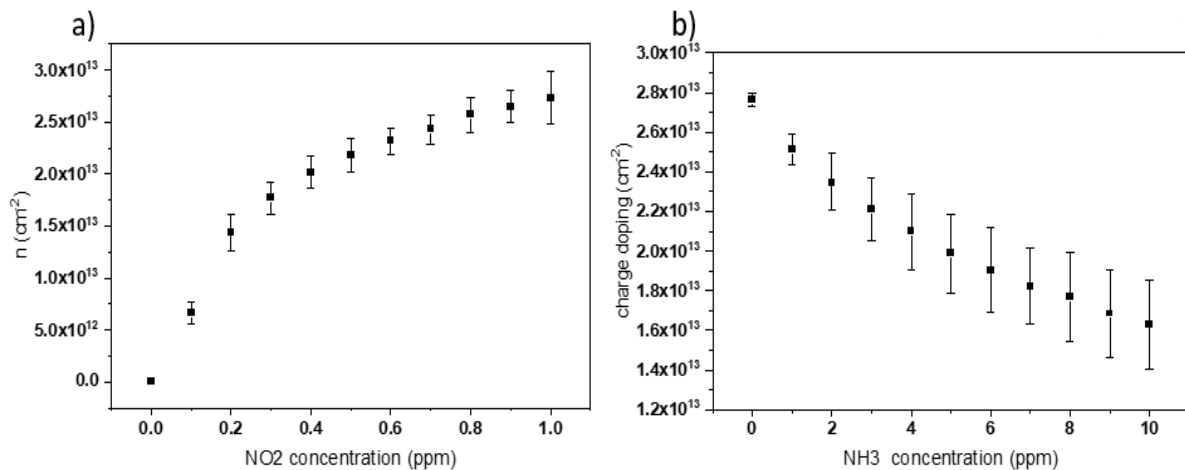


**Fig.4:** (a) represent the increment of the charge doping upon changing the NO<sub>2</sub> concentration. (b) the change of the charge doping with changing the NH<sub>3</sub> concentration.

In comparison with published results for GFET mobility which ranges from [5-9], our device mobility is close to the highest published mobility. Also, they reported the measurement by changing the gate voltage bias; they were able to variate the Fermi level and record the shift in the Dirac point. Comparing the GFETs fabricated within this work with those presented within the literature and by representing the shift in the Dirac point and change in carrier concentration upon gas adsorption, we showed that our GFETs are capable of detecting a shift in the Dirac point upon exposure to NO<sub>2</sub> and NH<sub>3</sub> at 0.1ppm and 0.5ppm respectively. Shifting in the Dirac point is attributed to molecular doping to the graphene channel.

#### 4. Conclusion

In this work, we have demonstrated high mobility GFET-based graphene chemiresistors. The doping of GFET by molecular can be tuned electrically by the back gate voltage. The charge transfer doping cause change in the Fermi level position relative to the Dirac point position. We demonstrated that the change in gas concentration of the oxidising gas (NO<sub>2</sub>) causes a shift in the Dirac point from 10V to 50V, while the reducing gas (NH<sub>3</sub>) shows a reverse shift in the Dirac point from 50V to 31V. This change is due to the change in the carrier concentration upon gas adsorption.

#### Acknowledgements

This work has been supported and funded by Jouf University and Saudi Arabian Cultural Bureau (SACB).

#### References

1. S. S. Varghese, S. H. Varghese, S. Swaminathan, K. K. Singh, and V. Mittal, "Two-dimensional materials for sensing: graphene and beyond," *Electronics*, vol. 4, no. 3, pp. 651-687, 2015.
2. K.-S. Kim *et al.*, "Chemical vapor deposition-grown graphene: the thinnest solid lubricant," *ACS nano*, vol. 5, no. 6, pp. 5107-5114, 2011.
3. B. Y.-K. Hu, E. Hwang, and S. D. Sarma, "Density of states of disordered graphene," *Physical Review B*, vol. 78, no. 16, p. 165411, 2008.
4. G. Neri, "First fifty years of chemoresistive gas sensors," *Chemosensors*, vol. 3, no. 1, pp. 1-20, 2015.
5. T. Wehling *et al.*, "Molecular doping of graphene," *Nano letters*, vol. 8, no. 1, pp. 173-177, 2008.
6. A. Singh *et al.*, "Electrically tunable molecular doping of graphene," *Applied Physics Letters*, vol. 102, no. 4, p. 043101, 2013.
7. J. Wei, B. Liang, Q. Cao, H. Ren, Y. Zheng, and X. Ye, "Understanding asymmetric transfer characteristics and hysteresis behaviors in graphene devices under different chemical atmospheres," *Carbon*, vol. 156, pp. 67-76, 2020.
8. F. Yavari, E. Castillo, H. Gullapalli, P. M. Ajayan, and N. Koratkar, "High sensitivity detection of NO<sub>2</sub> and NH<sub>3</sub> in air using chemical vapor deposition grown graphene," *Applied Physics Letters*, vol. 100, no. 20, p. 203120, 2012.
9. V. Blechta, M. Mergl, K. Drogowska, V. Valeš, and M. Kalbáč, "NO<sub>2</sub> sensor with a graphite nanopowder working electrode," *Sensors and Actuators B: Chemical*, vol. 226, pp. 299-304, 2016.
10. F. Urban, G. Lupina, A. Grillo, N. Martucciello, and A. Di Bartolomeo, "Contact resistance and mobility in back-gate graphene transistors," *Nano Express*, vol. 1, no. 1, p. 010001, 2020.
11. L. Lin *et al.*, "Towards super-clean graphene," *Nature communications*, vol. 10, no. 1, pp. 1-7, 2019.
12. R. S. Muller and T. I. Kamins, *Device electronics for integrated circuits*. John wiley & sons, 2002.